Abstract

Aurora is the Olin College Human Powered Vehicle Team's first entry into the ASME HPV single rider speed challenge competition. In order to build on past innovations in the field and avoid wasting time on well-studied problems, much of our time was initially spent researching the work of other human powered vehicle designers. Based on this, we chose to build a recumbent low racer in order to maximize rider flexibility, enable efficient riding posture, and minimize aerodynamic drag. The choice was also motivated by the availability of guiding research that could assist us in designing a successful vehicle.

Our design produced a simple, effective vehicle with a number of important technical features. These include a frame geometry centered on a long, horizontal main tube that facilitates integration of the frame with the fairing and allows for axial seat adjustability. The seat itself accommodates differently-sized riders by sliding along the main tube, secured by a quick release mechanism; this seat setup also allows the complete exchange of one seat for another without alterations to the frame. Our front wheel drive system minimizes weight and overcomes the complexity and reliability issues associated with more common rear wheel drive systems. Another notable feature is our double-pushrod steering mechanism, which maximizes rider knee space by displacing the handlebars from the head tube and eliminates forces on the handlebar support tube. Our steel tubular frame is both simple and robust, and aerodynamic drag is diminished with a three part fairing consisting of a fiberglass nosecone, a corrugated plastic midsection, and an angular tailbox. We plan for the *Aurora* to achieve a top speed in excess of 50 mph.

1 Design Process: Innovation and Inspiration

Our design process was separated into four major component subsections: frame, drive train, ergonomics, and fairing. The initial stages of design were accomplished with all teams working in parallel in order to arrive at a cohesive set of initial specifications and dimensions. After that point we began an iterative process in which refinements in each component set new specifications for every other component. This process allowed for the optimization of the vehicle as a whole by optimizing each component simultaneously.

We conducted two institution-wide design reviews, which were formal presentations to elicit feedback from the faculty and student communities on our design. These design reviews made it possible for us to consult more knowledgeable individuals who were not a part of the team to give us useful feedback as well as generate more awareness on campus of our project.

1.1 Initial Design Choices

We chose to enter the single rider event because we felt the design goals were clearer and we wanted to build a fast vehicle. After that, speed became the primary objective and was the driving factor through the rest of the design process. Along those lines, we chose a recumbent rider position over prone, which was ruled out as an uncomfortable position that impeded breathing. Two wheels were preferred over three for lower rolling resistance and the ability to corner at high speeds by leaning into turns. Both short wheelbase and long wheelbase designs were considered. We opted for a shorter wheelbase to benefit our turning ability and decrease wetted area of the fairing. For wheel sizes we selected a 700 mm rear wheel and a 16 inch front wheel. A larger wheel in the rear gives the ability to use a low friction road racing tire. Having already selected short wheelbase, we needed a front wheel that could fit comfortably between our legs and not interfere with the pedals when turning. A 16 or 20 inch wheel would have been appropriate, but we selected the 16 inch for an extra safety margin.

1.2 Frame

To begin the frame design process we defined our two major design criteria: the frame must be simple enough for the team to build with available shop experience and resources and it must be adjustable enough to maximize power and accommodate the dimensions of all of our racers.

We first considered frame geometry. After evaluating several designs in which the seat and its support members were built into the frame, we developed an innovative alternative design: a single horizontal steel tube spanning the distance between the two wheels enabling us to have a horizontally-adjustable seat mounted on quick-release brackets. This innovation makes it possible to quickly vary the distance from the seat to the pedals to be optimal for each rider by loosening only one quick release. This construction also means the seat is not built into the frame, and thus one seat design can be removed and replaced by another without modifying the frame.

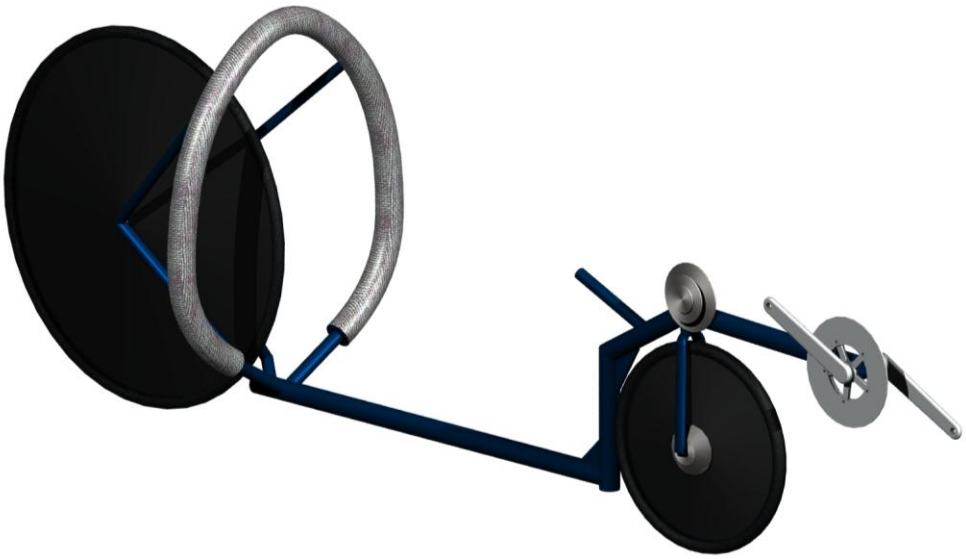

Figure 1: Prototype frame design.

In further support of our goal to support multiple riders, we evaluated a range of rake and trail relationships to optimize the stability of the *Aurora*. Rake and trail describe the angle of the head tube and the distance at the ground between the centerline of the head tube and a vertical line through the center of the front wheel. If either or both of these variables are too big, the bike will have sluggish steering and be difficult to control at low speeds. Inversely, if they are too small, the bike will be overly responsive to steering inputs, and thus difficult to control at high speeds. We initially used our knowledge of recumbent bikes and suggestions from our research to estimate optimal rake and trail. In general, longer trail provides greater stability and shorter trail gives greater maneuverability. Racing road bikes generally have trails in the range of 1.2 to 1.8 inches (Whitt). Compensating for the longer wheelbase of the recumbent we would want shorter trail, but at higher speeds, stability is greatly preferred. Within the HPV community, at least 2 inches of trail is expected for a racing HPV (Beauchamp). However, this value may be based on a straight course. We decided to use a trail of 1.5 inches for the first prototype.

At this point, we needed to choose a material from which to build our frame; our options included carbon fiber, aluminum tube, steel tube, and rectangular steel tube. We evaluated each of these possibilities on several axes:

	Carbon Fiber	Aluminum Tube	Steel Tube	Rectangular Steel Tube
Ease of Fabrication	1	2	4	4
Cost	1	3	4	3
Strength	4	2	3	4
Weight	4	3	2	2
Availability	2	4	4	1
Totals	**12**	**14**	**17**	**14**

Table 1: Decision matrix for frame material options.

Many of the designs we came across in our research used either carbon fiber frames or intricate aluminum or steel tube frames. Carbon fiber is the best frame material in terms of strength to weight, but it is also expensive and requires a certain level of expertise to achieve good results. We ultimately chose to simplify our design by using tubular metal construction rather than carbon fiber in order to maximize our resources in other areas including fairing production, drivetrain, and analysis. We chose steel tube over aluminum for superior fatigue resistance. Also, all of our previous welding experience was in steel, making it much more practical to use. Overall, we were more confident in our abilities to make a safe, reliable frame using steel tube rather than aluminum. We are interested in pursuing an aluminum frame in the future to improve frame stiffness, especially around the drivetrain.

The option of using rectangular tubes, particularly under the seat, was discussed, but ultimately rejected because our steel supplier did not sell a large enough steel tube with adequately thin walls, so our frame would have been heavier than desired. We chose instead to use circular 4130 chromoly steel with a wall thickness of 0.035 inches, which is reasonably light while still being easy to weld.

For our roll bar, we plan to use fiberglass rather than steel in order to decrease weight and improve ease of curve-fitting. Since we do not have a tube bender, fiberglass will enable us to create a curved profile, which is better in terms of both material efficiency and even load distribution.

1.3 Drivetrain

A well-designed drivetrain is a necessity in any successful HPV since efficiency of the drivetrain is directly related to the maximum speed a rider can attain. The team considered many options for maximizing efficiency and reducing manufacturing difficulty, and decided the front wheel chain drive would be the best for our needs.

Efficiency was our primary concern in the design of our drivetrain, but several other issues were considered, including ease of fabrication, ease of operation, and robustness. All of the potential designs, which included flex shaft, rear wheel drive, k-drive, and front wheel drive, were evaluated on these axes:

	Flex Shaft	Rear Wheel	Front Wheel	K-Drive
Ease of Fabrication	1	3	4	2
Ease of Operation	3	3	4	2
Robustness	3	3	3	1
Efficiency	2	3	3	3
Totals	**9**	**12**	**14**	**8**

Table 2: Decision matrix for drivetrain options.

A) Flex Shaft - Our most innovative design option used a flexible drive shaft to transfer power from the cranks to an internally geared hub on the front wheel. This design was based loosely on DynamicBicycles (www.dynamicbicycles.com), modern production bicycles using a shaft in the place of a chain. Conceptually, this design solved several of our most challenging problems. First, it eliminated complications involved in steering with the front wheel. The shaft could move to stay clear of the spinning wheel and any resultant shaft rotation would be transferred to the wheel without noticeably affecting the pedal stroke. This design also solved the issue of accommodating various riders. There is a four-inch difference between the inseams of our tallest and shortest riders,

which must be accounted for somewhere in the frame. A flex shaft drivetrain would allow the front boom to be extended or shortened for different riders, something that would be much more difficult with a chain drive which needs a fairly constant distance between the driving and driven gears. Three issues weighed heavily against this option: 1) the difficulty of fabricating the gearboxes required to greatly reduce the torque in the shaft, 2) the challenge of integrating the gear boxes with the crankset and internally geared hub and 3) the much greater frictional losses in the shaft housing and lack of torsional rigidity. Despite these, we think this design still holds promise and we plan to explore it further in future years.

B) Rear Wheel Drive - This is the drivetrain most commonly used on recumbent bicycles. It has advantages in its similarity to a standard bicycle drivetrain, thereby increasing the availability of standard components. Bicycles equipped with this sort of drive mechanism often suffer from increased weight due to the length of chain and a softer pedal stroke due to chain slack and movement in the pins. With our low-racer frame design, rear wheel drive would have required a complicated and inefficient system of rollers to route the chain from the crankset over the front wheel, under the rider, and up to the back wheel. Additionally, we expected our long, single tube frame to have a significant amount of built-in suspension, which would noticeably and negatively affect the drivetrain if it were to be routed along the frame.

C) K-Drive - We also considered implementing a K-Drive style crankset for a potentially more efficient elliptical pedal stroke and a smaller fairing foot area for better aerodynamics. The crankset was fully designed, but ruled out due to lack of robustness. The aerodynamic advantage would not be worth the lost time due to an almost certain failure of the K-Drive sometime during the race.

D) Front Wheel Drive - Like rear wheel drive, front wheel drive uses largely standard bicycle components, but adds significant complication to the system by having the driven wheel also turn. The option of rear wheel steering was briefly considered, by rejected due to the difficulty of riding such a bicycle. For the chain to track properly, chainline movement should be reduced to axial twisting. The method often used to address this problem in other racing HPVs is to use two drivetrains connected through an interchange called a jackshaft, which is located near the head tube. This makes one chainline stationary and restricts the other to axial twisting. This more compact drivetrain helps address the issues of excessive chain weight and drivetrain rigidity. Front wheel drive introduces its own routing complications due to steering, but they are easier to overcome.

Our Design

The initial design for the drivetrain was a simple front wheel drive using dual chain drives. We attempted to minimize the complexity of the whole drive system, using only one derailleur on the driven wheel and one additional chain tensioner. The drivetrain is geared up at the jackshaft about 2.5:1 to allow for higher than normal speeds, despite a smaller wheel. Theoretically, the gearing allows for a top speed of 54.7 miles per hour when pedaling at 100 rpm. Chain routing immediately became an issue since the chain often jumped off the driving sprocket on the jackshaft with even the slightest turn of the wheel. The first solution was a roller to hold the chain in line onto the sprocket, as shown in Figure 2b. This was later replaced by plates on either side of the sprocket to ensure that the chain couldn't accidentally slip off, Figure 2c. This design gave a smoother, quieter pedaling action, suggesting greater efficiency. Also, the plates were capable of guiding the chain in both directions, so reliability in backpedaling was greatly increased. In testing, though, the plates failed to retain the chain in the full range of gears. In fact, in the higher gears the plate seemed to help lift the chain off the sprocket. Given this, we reverted to the roller design. It may be that the best solution will be a combination of the roller and plates.

a) No guiding mechanism b) Chain Roller c) Guiding plates

Figure 2: Various methods of guiding chain through the jackshaft.

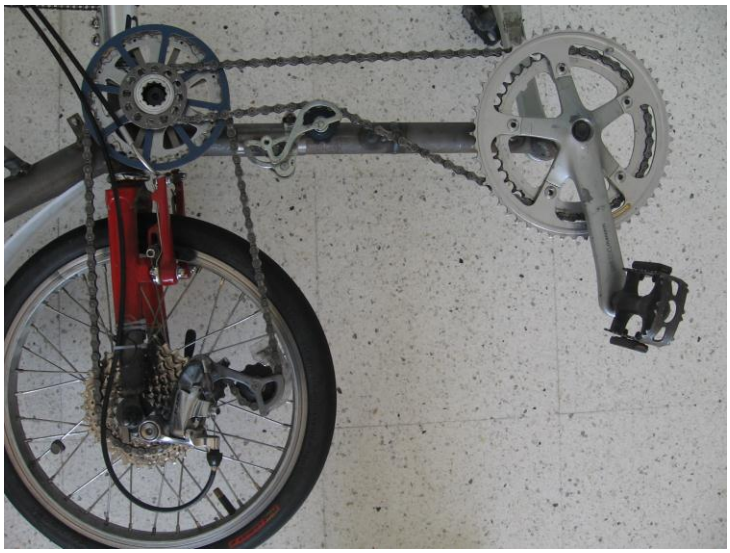

Figure 3: Full drivetrain.

1.4 Ergonomics

The performance of a high-speed HPV is heavily dependent on both the rider and the vehicle. As such, we attempted to maximize rider comfort and pedaling power through an effective rider position and seat design. The first design criterion we considered was the seat angle. We initially planned to conduct tests for different seat configurations to determine which seat angle was best for power output. However, our research indicated that the most important factor for pedaling power is a rider's familiarity with a certain angle, not necessarily the angle itself (Wilson, 85). We therefore chose the angle based on rider comfort and what best fit with our frame and fairing designs. Additional criteria for the seat included allowing for an adjustable angle for easy prototyping and a seat that could slide along the frame to accommodate different rider sizes.

We evaluated several seat angles for comfort. In order to determine the comfort of different seat angles, we built a wooden seating jig. We also used this jig to take pictures of and measure the pedaling area, which was useful for designing the fairing. We tested riders pedaling at a variety of angles and determined by a consensus of subjective rider responses that a lower seat angle is more comfortable. In addition, a lower seat angle is more aerodynamic because it allows the fairing to be smooth rather than bubble up to make room for the rider's head. Unfortunately, this design requires that a window be built into the fairing.

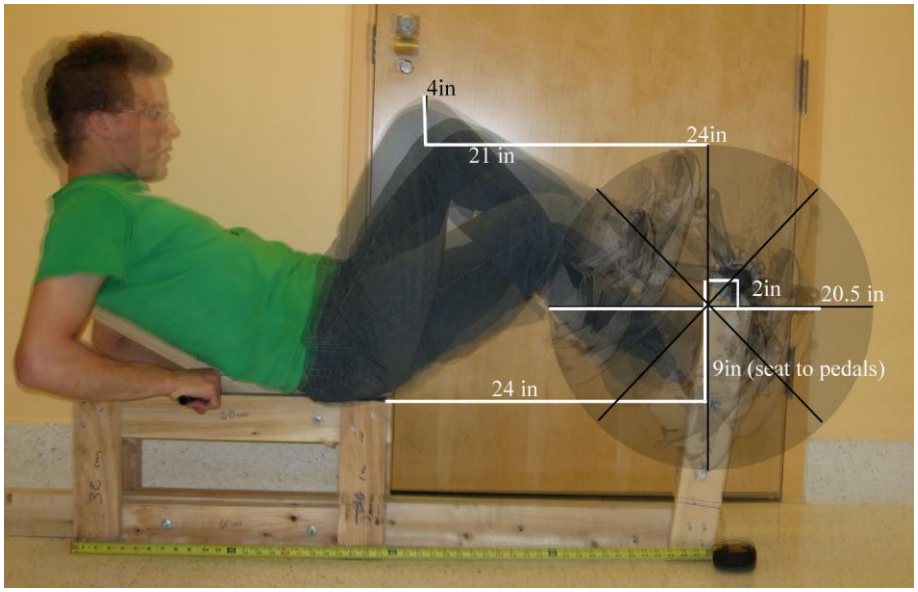

Figure 4: Pedal stroke testing with seating jig.

Our first seat prototype was constructed of wood, backed by aluminum, so the entire back of the rider could be supported with minimal weight and the greatest building simplicity. Using an aluminum channel reduced the number of parts we needed to manufacture by combining the structural support and the mounting points. With this seat it was easy to adjust the seat back angle and distance to pedals to test various positions, but it was not comfortable, light, or strong enough to be our final seat. After determining an appropriate position with the fully adjustable seat we designed a final seat. This final seat will incorporate steel tubes, a mesh back, and welded construction. Because the tubes will be welded, the seat back angle will not be adjustable, but the rigidity of the seat will be greatly increased. It will still be adjustable for the leg lengths of different riders using a single quick release, allowing adjustments in minimal time. In the final model, there will be a bracket on the rear seat mount which will slide on rails and provide torsional stability. This bracket was an innovation of our own design, which solved the issue of the seat shifting from side to side without compromising the ease of adjustability.

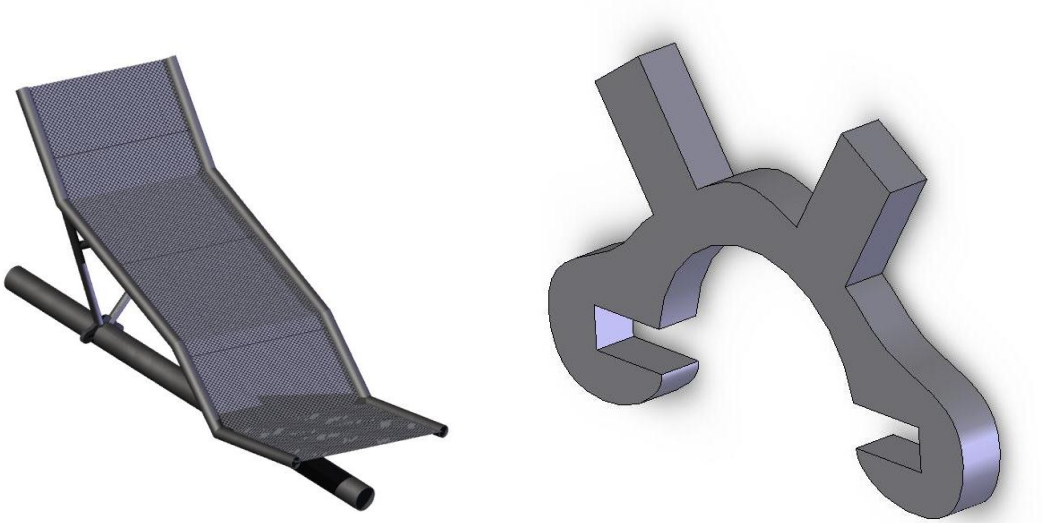

a) Seat design with form fitting curvature

b) Rear seat bracket

Figure 5: Seat design with torsionally stabilizing rear bracket.

1.5 Fairing

For our fairing design, we took inspiration from living and mechanical systems, combining styles to produce creative designs. We began working on a full fairing by modeling in 3D CAD programs, and performed various analyses. We ultimately settled on the concept of a nosecone covering only the front portion of the vehicle (and bearing the majority of the air pressure), a plastic midsection, and a tailbox.

Ideation claimed the majority of our fairing construction timeline. We began with some designs that have been attempted in the past, looking at the Varna Diablo and other successful human powered vehicles. Our team had limited experience in the field of aerodynamics, so we studied books on airplanes, wing design, and automobile dynamics. We came across a promising and newly popularized strategy for finding creative aerodynamic shapes: looking to specific animals in nature for their shapes. A prime example is Mercedes-Benz's boxfish-inspired bionic car: a successful implementation of biomimicry in vehicle design. Mercedes adapted the form of a creature that lives in a viscous environment to make it fit their design needs. We explored this possibility, especially pursuing the shape of a diving peregrine falcon. The peregrine falcon has been recorded as the fastest creature on Earth at top diving speeds of 240 mph. After researching extensively, it was decided that the falcon evolved according to different design parameters. Of these, an easily identified difference is the bird's minimal constraints on any ratio of dimensions in its body shape, whereas we need the ratio to be approximately a person's height over their width. Additionally, the bird requires a bulk of sensory equipment at the front of the body (i.e. in the head), whereas we had no real use for a formidable bulge in the shape of a bird's head at our feet. We found too few images of falcons to use it as a base model, so the strictly peregrine design was dropped, but some ideas from its ideation were retained.

The fairing team worked largely in SolidWorks to create a 3-dimensional design. We had a few design requirements that were critical to follow, given to us by different task groups on our team. From the ergonomics team, we were given a full sized computer model of a person and an egg-shaped pedaling region that had to be fully encompassed by the fairing. Our basic shape then assumed a bullet shape of length roughly equal to a fully extended rider. Our design also took the frame into account, paying attention to the proximity of the fairing to the ground and attachment points to the steel tubing. As for the main guidelines we followed in shaping the fairing, we valued most highly a shape that had no concavities. Constant change in curvature was a priority over constant curvature itself, leading to a semi-parabolic shape. On the rear end, it was decided that we should taper to a vertical line in order to encase the wheel completely. Although it did not play a role in this portion of our design, cost was also an important design constraint. We ended up with three main designs—one with a bubble canopy to house the rider's head, one with a bulging front end, and one that positioned the head at the level of the rider's knees.

In terms of cost considerations, we then evaluated the relative benefits of a full fairing compared to a partial fairing. Although the latter was more cost efficient, we were worried about the flow of the air once it had reached the end of the fiberglass nosecone. However, our research indicated that laminar flow, if achieved, would cover approximately the first 30 cm of fairing before deteriorating into turbulent flow (Carroll). This meant that the exact smoothness of the majority of the body would not be critical, and we could replace the long flat portions of our fairing with panels of bendable corrugated plastic called Coroplast. The full fairing also produced issues concerning entrance and exit of the vehicle; these would not be a problem if the nosecone was attached to the frame and we used the plastic midsection as a hatch. Another benefit from the smaller scale project was the lower cost and faster pace of prototype construction. In the end, we went with the more cost efficient option, and began working on our previous designs to adapt them for use as partial fairings.

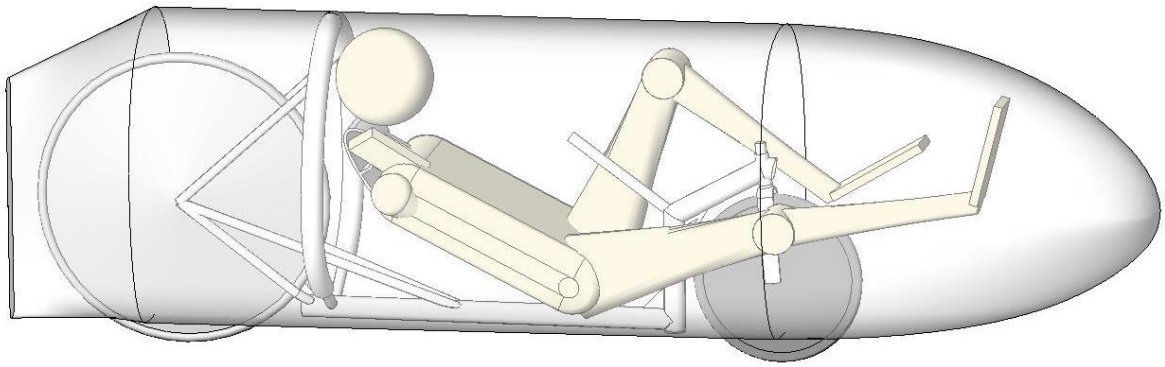

Figure 6: Fairing design with nosecone and plastic midsection and tail.

1.6 Controls

After establishing these four components, we concentrated on the bicycle control.

Steering - The first priority in steering design was to minimize the learning curve as much as possible by using a simple, easy-to-use steering mechanism. This would allow as many riders as possible to ride it in various conditions. We considered several different options, including standard handlebars, tiller steering, chain drive, and a double push rod. After building the first frame with standard handlebars, we realized that although they offered good sensitivity and control, they impeded the rider's knees from forming a smooth pedal stroke. To correct this, we implemented a tiller steering system. Though difficult to control, the tiller steering significantly increased the rider's knee space. However, it was ultimately too difficult to use; only two riders were successfully able to ride it. As such, we tried chain drive steering. The handlebars were supported with a slightly flexed tube that was intended to tension the steering chain. This steering method was much easier to control than the tiller, and it also provided sufficient knee space. However, the tube that was supporting the handlebars was able to bend too much, causing slack in the chain during hard turning, shown in Figure 7. This meant that we could effectively only steer while the vehicle was moving. We finally chose to use a double push rod steering mechanism. It is possible to steer with a single push rod, but, as demonstrated in Figure 8, this would have put essentially the same forces on the support tube. The problem is avoided most effectively with a double pushrod mechanism, giving a highly stable four bar linkage.

Figure 7: Chain steering mechanism showing slack while turning.

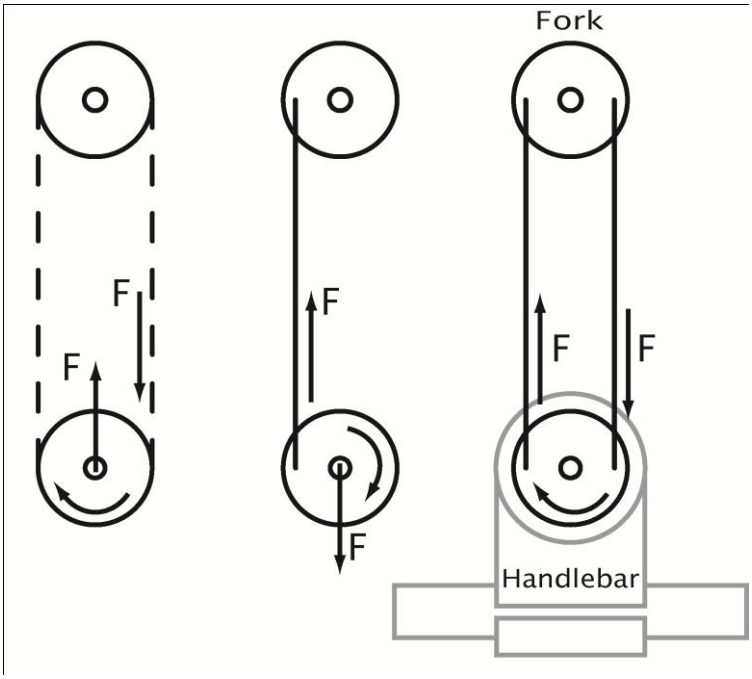

a) Chain drive b) Single push rod c) Double push rod

Figure 8: Variations of remote steering mechanism.

Handlebars - We decided to use parallel, vertical handgrips rather than the flat handlebars typical of a bicycle. The vertical orientation of the hands encourages the driver to hold his or her elbows close to the body, minimizing interference with the legs. The pushrods further prevent interference, by allowing riders to steer large angles without the large displacements that occur with tiller steering.

Braking - The brakes were chosen fairly late in the process and so the decision was governed mostly by other predetermined factors. We opted to use only front brakes. 60% of the weight of the vehicle and rider is on the front wheel and would shift even further in that direction when braking, up to 100%. A rear brake could not apply a significant amount of stopping power before skidding. The center of mass is low enough that there is little risk of the rear wheel lifting off the ground, even when braking only with the front wheel. We selected V-brakes because they are very powerful, especially for their weight, and fit our needs very well. However, a set of standard V-brakes was too tall to fit under our drive train, so the left brake arm needed to be shortened. This had a small negative impact on our available braking power because it shortened the lever arm, but the brakes were still impressively powerful.

2 Analysis

To optimize our designs for speed and safety we analyzed them using various tools including hand calculation, finite element analysis, and computational fluid dynamics.

2.1 Roll Bar

In order to minimize the weight of our roll bar, we plan to construct it from fiberglass rather than steel. To determine the appropriate size of fiberglass roll bar to meet safety requirements, we compared it to a steel tube using static analysis. Hand analysis was the most appropriate tool to use because of the simple tubular geometry of the roll bar. We defined equivalent safety as the ability to support an equivalent bending load before failure. The mode of failure for either of these tubes would be excessive normal stress at the top or bottom of the tube. Therefore, we started with the bending normal stresses at these locations.

$$\sigma_{xx} = \frac{P \cdot d \cdot r}{I} \tag{1}$$

where P is the load applied, d is the span, r is the radius of the tube, and I is the cross-section moment of inertia. By rearranging, we equate the loads carried by each tube at yield stress.

$$P = \frac{y_{steel} \cdot I_{steel}}{r_{steel} \cdot d} = \frac{y_{fg} \cdot I_{fg}}{r_{fg} \cdot d} \tag{2}$$

Next, we expand I_{fg}.

$$\frac{y_{steel} \cdot I_{steel}}{r_{steel}} = \frac{y_{fg} \cdot \frac{\pi}{4}(r_o^4 - r_i^4)}{r_o} \tag{3}$$

Again, rearranging, we find the required outer radius of the fiberglass tube given the inner radius, which is predetermined by the size of the mold tube.

$$\frac{r_o^4 - r_i^4}{r_o} = \frac{\sigma_{y\ \ steel}}{\sigma_{y\ \ fg}} \cdot \frac{I_{steel}}{\frac{\pi}{4} \cdot r_{steel}} \tag{4}$$

Now, by supplying known values, we solve for the required outer radius. Yield stress for 4130 steel was found on MatWeb and the yield stress for fiberglass was provided by Aeropoxy with a safety factor of 3 to account for the possibility of inconsistent layup.

$$\frac{r_o^4 - (0.9375[in])^4}{r_o} = \frac{75000[psi]}{15057[psi]} \cdot \frac{0.05885[in^4]}{\frac{\pi}{4} \cdot 0.75[in]} \tag{5}$$

$$r_o = 1.0687[in] \tag{6}$$

The analysis sets the size of the fiberglass tube at 1.875” ID, 2.137” OD, and 0.130” wall. This tube will require 5 layers of fiberglass and will be approximately 55% lighter than the equivalent steel tube.

2.2 Frame

Having chosen a frame material and geometry, we set out to refine the details. Our main questions concerned the optimal size of steel tubing, strongest joint design, and effects of gussets. We used beam element analysis on tubes of 1.5,” 1.75” and 2” to determine the optimal size. After choosing the optimal tube size, we explored the structural implications of a mitered joint as compared to a fish-mouthed joint at point D (shown in Figure 9). Finally, we determined the effectiveness of gussets at increasing our factor of safety (FOS). Overall, our goal was to reduce the weight of the frame where possible while maintaining a FOS of just over 1.5.

We conducted preliminary frame analysis in ANSYS using beam elements. We used this primarily to determine an appropriate tube size for the frame geometry. Although this type of modeling is most inaccurate at joints, where the highest stresses occur, the analysis still identifies the highest stress joints, and gives us a basis for choosing an appropriate tubing.

The loading cases for ANSYS are given in Table 3 and the results from ANSYS are given in Table 4. Note that the only stresses that have a FOS lower than 1 are located at the rider position and result from inaccuracies in the loading case. In reality, the forces and moments do not act at points, and therefore would not cause such high stresses. Aside from that, the 1.5 inch diameter, 0.035 inch wall thickness tube has an overall FOS of 1.11. We concluded that this was the lowest acceptable FOS value for our purposes; lower values would provide weight savings of only a fraction of a pound while risking structural deformation. A stronger tube would be heavy and inefficient, especially since the joints, where the maximum stresses occur could be more significantly strengthened with gussets than with larger tube.

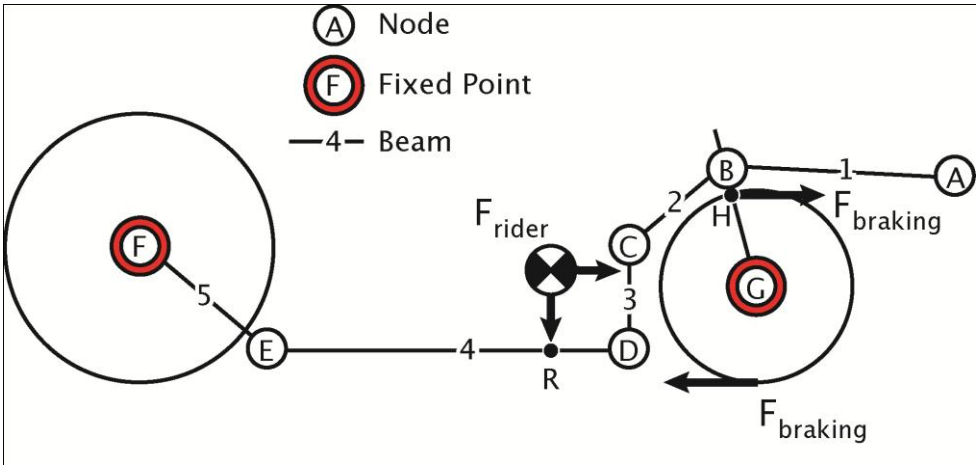

Figure 9: Frame loading for ANSYS FEA. Stress was calculated at the weakest points in the geometry, i.e. the joints and loading point R. The rider exerts a localized weight force on beam 4 and a braking force acts at node H.

ANSYS

	Force X	Force Y	Moment
H	135 lb	0 lb	0 lb-in
R	135 lb	530 lb	857 lb-in
F	Fixed	Fixed	Free
G	Fixed	Fixed	Free

Table 3: Loading cases for beam element analysis in ANSYS.

1.5 in				
		Stress		
Beam	**Point**	**Max**	**Min**	**FOS**
2	B	43559	-39411	1.721803
2	C	67185	-63289	1.116321
3	C	67182	-63293	1.11637
3	D	38443	-34554	1.95094
4	D	37625	-35372	1.993355
4	R	98208	-95955	0.763685
4	R	84181	-80224	0.890937
4	E	7676	-3719	9.770714

1.75 in				
		Stress		
Beam	**Point**	**Max**	**Min**	**FOS**
2	B	25390	-22301	2.953919
2	C	47579	-44482	1.576326
3	C	47707	-44354	1.572096
3	D	35752	-32399	2.097785
4	D	29045	-27406	2.5822
4	R	73532	-71893	1.019964
4	R	63437	-60342	1.182275
4	E	2760	334	27.17391

2 in				
		Stress		
Beam	**Point**	**Max**	**Min**	**FOS**
2	B	17713	-15154	4.234178
2	C	35513	-32948	2.111903
3	C	35704	-32757	2.100605
3	D	23789	-20842	3.152718
4	D	22946	-21685	3.268544
4	R	56962	-55702	1.316667
4	R	49375	-46843	1.518987
4	E	1868	663	40.14989

Table 4: ANSYS beam element results comparing tubing diameters. Results show that 1.5 inch tubing is the preferred choice because it is the lightest tubing that meets the required FOS. Note that the FOS for beam 4 is less than 1.0, but this result is due to loading inaccuracies. Realistically, point R models a human load as a point load and moment. Stress units are in psi, and the maximum yield stress of the material is assumed to be 75000 PSI.

After concluding our preliminary frame analysis, we conducted in-depth analysis of the joints with the highest stresses. To do this, we used SolidWorks COSMOSWorks FEA tools. To accurately construct the geometry, we made surface models in SolidWorks and used thin shell elements to mesh the shapes.

Analyzing our full frame design using FEA would have required a complicated model, making it difficult to troubleshoot, as well as being computationally intensive. Therefore, we focused on regions of high stress, the joints. We divided the frame into subsections centering on each of the main joints and applied statically equivalent loads. This type of modeling increased the efficiency of our analysis while sacrificing some accuracy. However, during analysis, the loads and restraints were applied a distance from the joints, which, under Saint Vincent's principle, is enough that any local loading inaccuracies would not effect the joint. Thus, the results we found were still valuable, and we were able to draw conclusions from them.

The difficulty of modeling was also reduced by using shell elements rather than solid elements for the joint analysis. Using solid models would introduce two major difficulties. Using a mesh that is a reasonable size given the diameter and length of the tube would result in elements far thicker than the wall thickness, which then would behave in a manner uncharacteristic with their physical counterparts. Compensating for that effect would require an overly fine resolution and therefore use an unreasonable amount of computing power. The shell mesh approach is more efficient and consistent with the physical characteristics of our frame.

To decide on the best joint to use at point D, we calculated the resultant loads the section of tube around the joint under the worst case loading conditions. The end of the joint closest to the front of the frame was loaded, and the other end was set as a fixed restraint, which is statically equivalent to loading both ends.

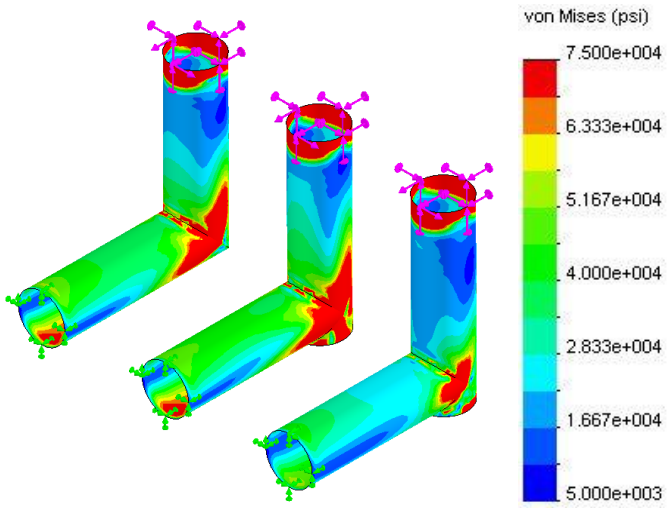

Figure 10: The results of our test for joint D. Von Mieses Stresses are measured in psi; the yield strength of the material (75 ksi) is shown in red. The mitered construction is on the left, the uncapped fish-mouthed tube is in the middle, and the fish-mouthed joint with end cap is on the right.

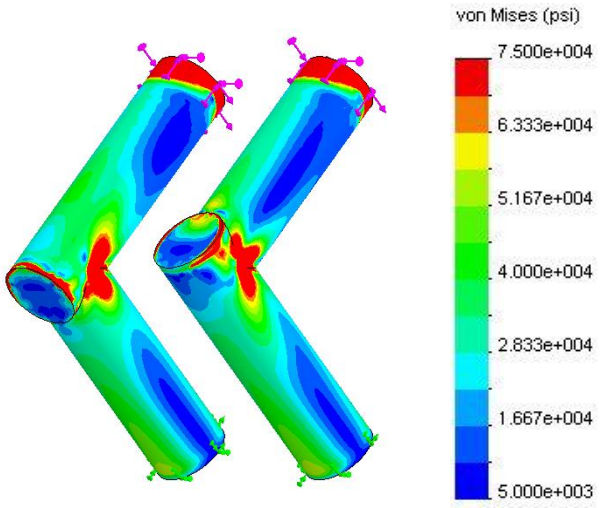

Figure 11: Again, stress are Von Mieses, and indicated in psi. Stresses beyond the yield strength of steel are shown in red. This shows the results of the joint configuration test. Although the orientation of the stress concentrations differs between the two, they are extremely comparable. Therefore, we made our decision based on fabrication concerns

The results of this test can be seen above. Figure 10 shows the resulting stresses, which confirm our initial intuitions about the relative strength of the joints. The much larger red areas indicate the higher stresses seen by the mitered and uncapped piece. While the mitered and unsupported fish-mouthed constructions have extremely similar stress characteristics, the capped fish-mouthed construction is clearly superior to both of them.

After determining the superiority of the capped fish-mouthed piece, we investigated the effect of different construction configurations to see what effect the orientation of the fish-mouthed joint had on its strength. As shown in Figure 11, there was little or no difference between them. Given that, we chose to cut tube 4, as it eased fabrication to have a positive stop.

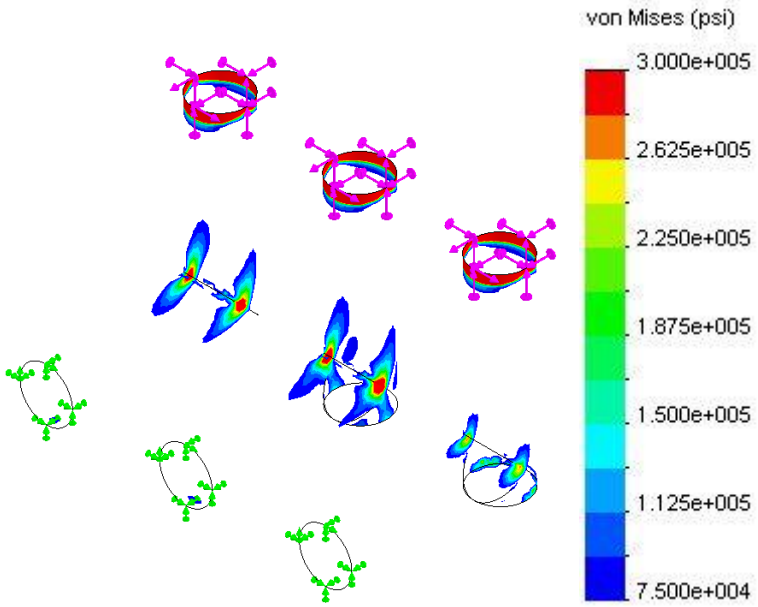

Figure 12: Joint stresses in excess of yield stress. It is immediately visible that very large areas, even in the strongest model, are beyond the yield strength of the material.

After looking at the results from the previous analysis, we saw that we had significant problems with the stresses the material was seeing. Figure 12 shows another view of the same test, this time isolating the areas experiencing stresses beyond the yield strength of the material. Even using the stronger construction, large portions of the material are beyond their yield strength. In order to counter this, we explored the use of gussets.

In order to determine the stresses on the joints, we created models of each joint, including the gusset. We used shell elements again, with the exception of the gusset in D, which, in order to support the jackshaft, would be too thick for shell elements to model accurately. Schematics of these models can be seen in Figure 13. Table 5 lists the loading cases used for each model; the rear end is fixed, and the front end is given loads statically equivalent to those on the front wheel.

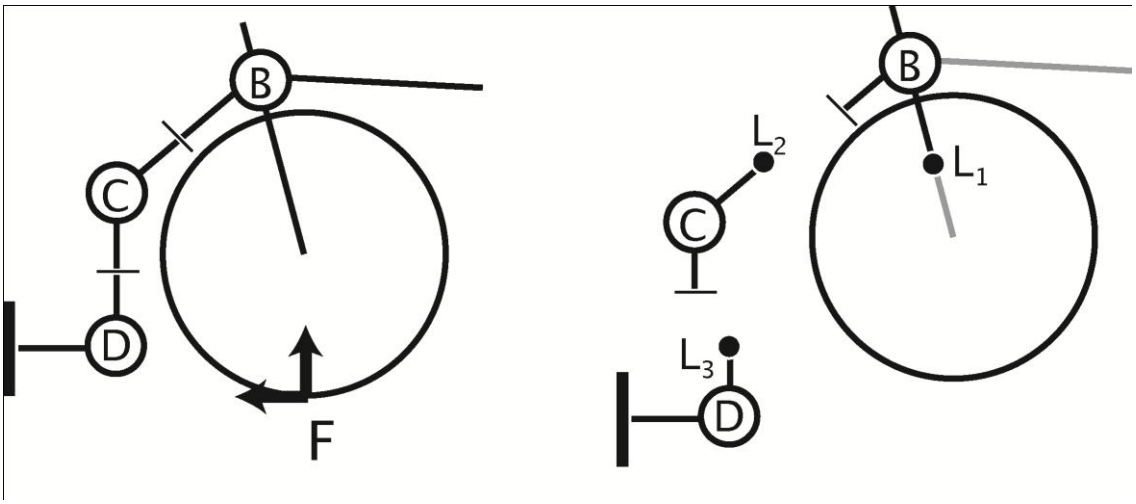

Figure 13: Frame loading on frontal joints for COSMOS FEA testing.

COSMOS

	Force X	Force Y	Moment
Initial Assumptions			
F_{normal}	0 lb	380 lb	0 lb-in
$F_{braking}$	135 lb	0 lb	0 lb-in
Particular Loading Cases			
D	135 lb	380 lb	2240 lb-in
C	135 lb	380 lb	-300 lb-in
B	135 lb	380 lb	-1430 lb-in

Table 5: Loading Cases in COSMOS. Used to load the ends of the models in COSMOS.

.

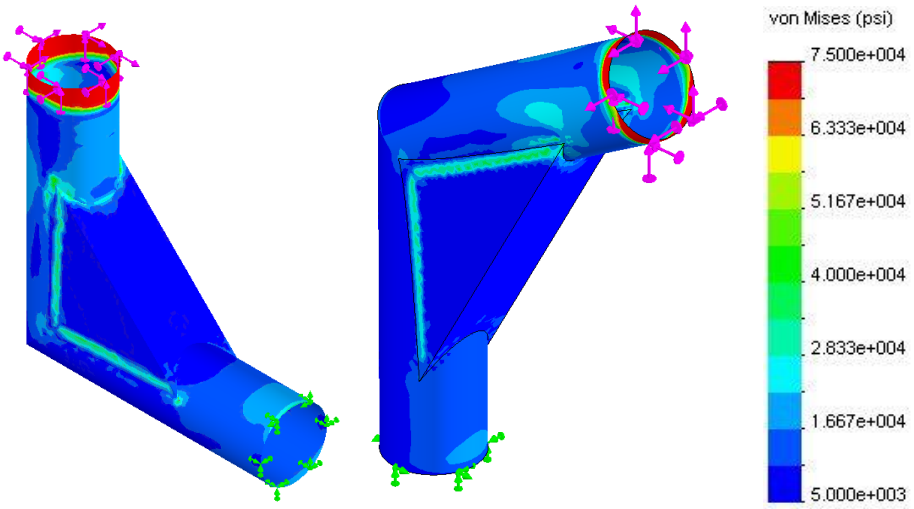

Figure 14: Results from FEA using COSMOS. Joint D is on the left, joint C shown is shown on the right. Shown are Von Mieses Stresses, in PSI. The highest stresses occur where the edge of the gusset intersects the tube. These parts both have an FOS of at least 1.5; this does not take into account the weld beads in the physical model, which act as fillets that would reduce stress concentrations.

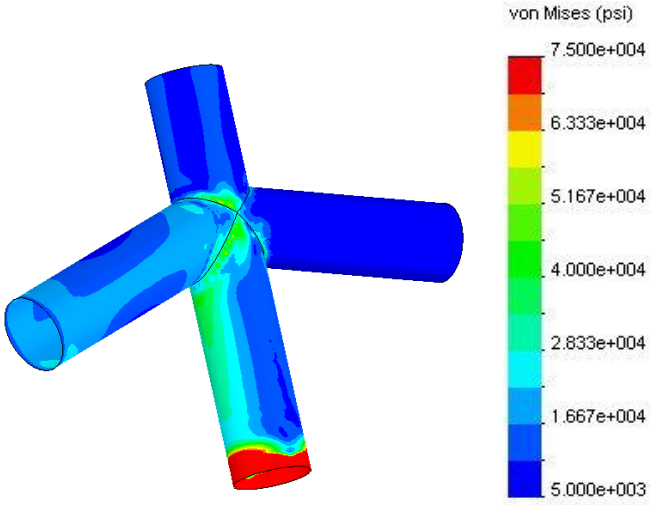

Figure 15: Results from FEA using COSMOS. Shown are Von Mieses Stresses, in PSI. The highest stresses occur at the juncture of the tubes. Note that this joint has a sufficient FOS without a gusset, although we considered one in order to stiffen the joint

The results for these tests can be seen in Figures 14 and 15. Joints C and D, shown in Figure 14 respectively, have extremely similar characteristics. They both exhibit stress concentrations where the edges of the gusset intersect the tube. At these concentrations we see our lowest FOS for the frame, of 1.5. It is reassuring to note that these stress concentrations are higher than those actually experienced by the frame at that point, due to the nonzero thickness of the weld bead

Joint B has a slightly different case. The short length of the tube at gusset D doesn't allow us to load it where it ends. Instead, we assume that lengthening the head tube and loading it at a different point will yield comparable results. With this joint, as shown in Figure 15, it is important to note that the ungusseted joint is sufficiently strong. This is useful, because spaced around the joint is too tight to allow us to place much of a gusset there. We did consider the use of short shear plates to help stiffen the joint. Figure 16 shows the results of this test; while it certainly reduces the displacement, stiffening the frame, the change is not significant.

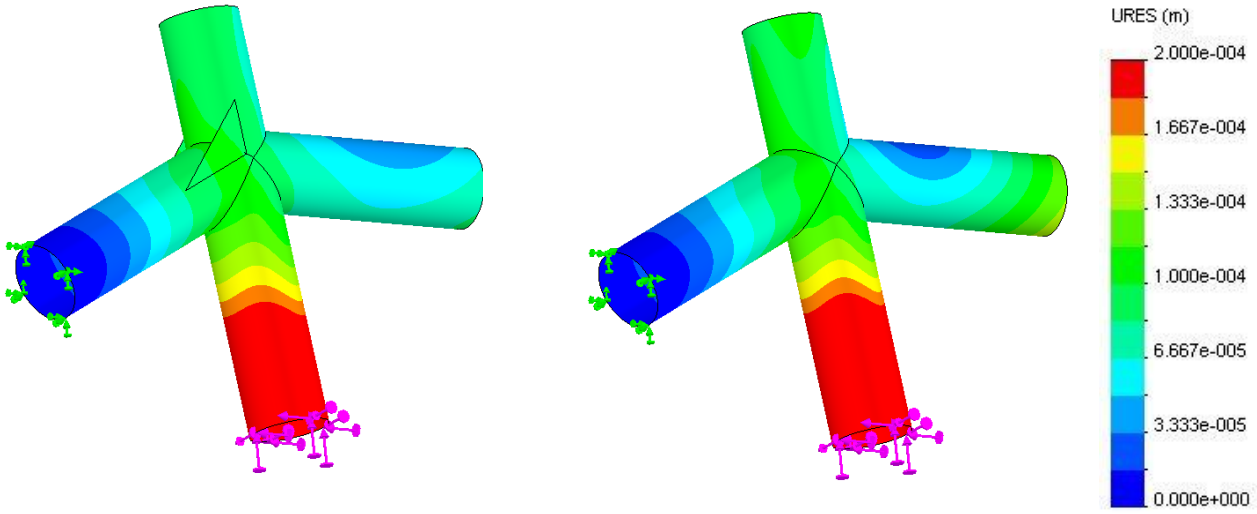

Figure 16: This shows the results of testing stiffness with and without a gusset at the joint

We next examined the tube between joints C and D. We were concerned that a stress concentration might occur as a result of the gussets, creating high stresses. The loading case is very similar to joint C, with the exception that the rear side of joint D is fixed, rather than the rear side of joint C. No such stress concentration was found, as shown in Figure 17

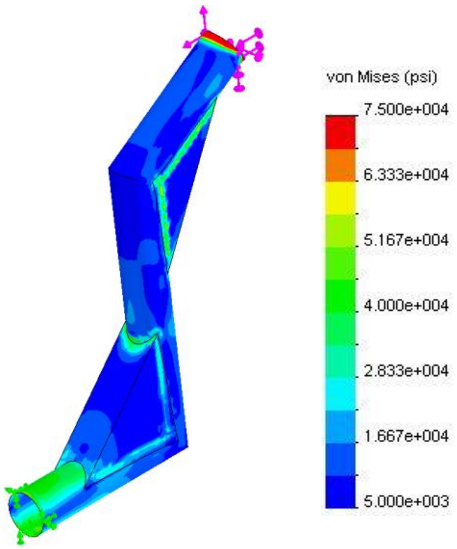

Figure 17: Shown here are the results of our testing for other stress concentrations. Stress is indicated in von Mieses psi, with anything above the yield strength of the material (75,000 psi) in red. The results are very similar to previous segmented models, confirming our analysis.

2.3 Fairing

To begin analysis of the fairing, we chose three variations of our basic design: minimal curvature, front bulge, and canopy (pictured in Figure 11). COSMOS FloWorks was used to visualize the flow around each geometry at a constant Reynolds number (Re) of 2.99 x 10^6. Our fairing designs were modeled around the same frame, so they all had nearly identical characteristic lengths; as such, this Re corresponded to a wind speed of about 15 m/s (33.5 mph). We found that the low-curvature design had higher average pressure than the canopy design, but had the lowest C_dA value of all the designs (about 0.0135 m^2). This is lower than the Varna Diablo's calculated C_dA of 0.020 (Beauchamp), which initially raised doubts about the validity of our results. However, the Varna's C_dA calculation considers drag generated by the wheels, which our model fails to do. Also, our other fairing designs had drag coefficients that were more comparable to those of existing vehicles, which helped to validate our data. The front bulge design had a C_dA of about 0.027 m^2 and experienced a notable low pressure zone right behind the bulge, as seen in Figure 10c; the canopy design had negligible low pressure zones, but experienced overall higher pressure per unit area than the smooth fairing; its C_dA was also about 0.027 m^2.

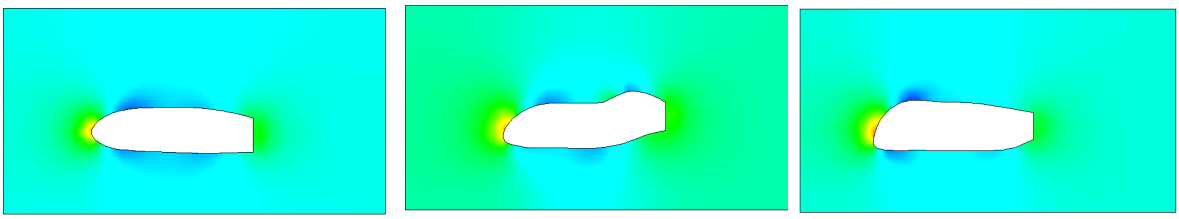

a) Low curvature b) Canopy c) Front bulge

Figure 18: Pressure distributions for fairing designs: a) low-curvature (max pressure = 101431 Pa), b) canopy (max pressure = 101429 Pa), and c) front bulge fairings (max pressure = 101459 Pa).

Low pressure zones are problematic because they lead to boundary layer flow separation, which contributes to wake drag. By having a relatively constant pressure distribution along the length of the fairing, we hoped to keep the flow attached and increase laminar flow. However, operating conditions for an HPV are not conducive to laminar flow, as water droplets, mud, and vibrations from the road tend to trip the flow and cause turbulence (WISIL). This largely renders low pressure zones a non-issue, since we cannot really expect laminar flow anyway. Additionally, we used average pressure mostly as a qualitative indicator of drag coefficient. Since we were able to quantitatively determine more informative C_dA values (albeit for an idealized conditions), we decided to weigh pressure less heavily as a design factor.

As mentioned earlier, we neglected to consider drag generated by the wheels. Wheel components such as the rim, spokes, and hub tend to disturb airflow, which increases effective drag coefficient; ideally, we should have considered their effects on C_dA. However, since all of our fairing designs leave an equal portion of wheel exposed, we assumed that their effects would be fairly constant for each model, and could therefore be ignored. To some extent, this assumption is not entirely valid, since various fairing shapes direct air flow differently, meaning that the flow about the wheels does not necessarily behave identically. However, our models are very similar in the lower half since they were closely fitted to rider measurements. Also, we made the nose relatively close to the ground in order to avoid a Venturi effect, so most of the air should have been directed laterally rather than under the vehicle.

Based on these criteria, we decided to pursue minimal curvature as the main design for our fairing. Although the canopy design had less drastic low-pressure zones than the other designs, we decided to weigh drag coefficient and average surface pressure more heavily as design criteria; this is because the airflow across a faired vehicle generally becomes turbulent about 30 cm behind the nose (Carroll), which would essentially make flow separation a non-issue.

In order to optimize the low-curvature design, we varied the nose height and used COSMOS FloWorks to calculate the average normal force acting on each version. We found the nose height at which the normal force on the fairing was lowest, yielding a C_dA value of 0.0135 m^2. With a cross-sectional area of approximately 0.3 m^2, this means that our calculated drag coefficient is about C_d=0.045.

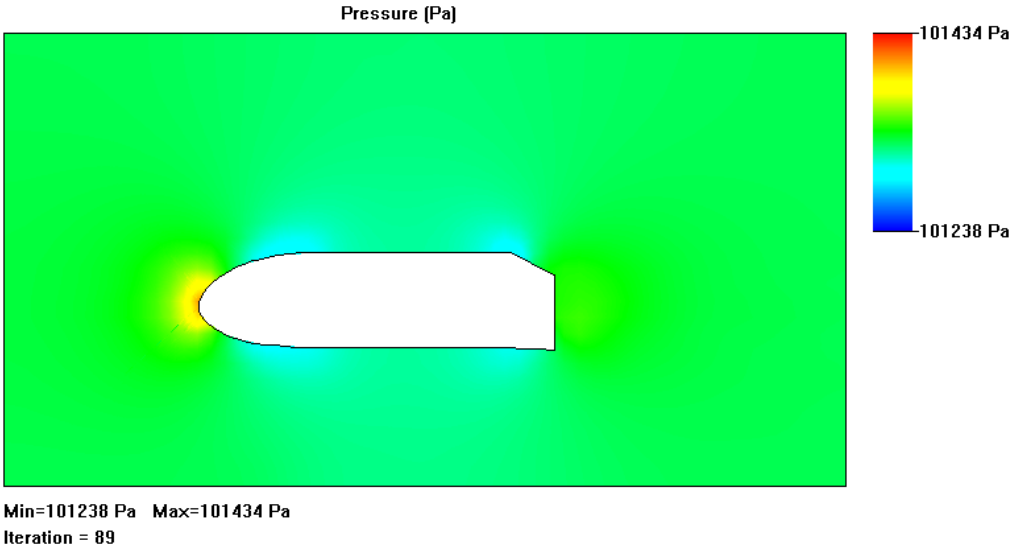

Figure 19: Nosecone with Coroplast cylinder and angular tail end.

As mentioned earlier, we ultimately decided to build a nosecone rather than a full fairing for several reasons, including limited funds and lack of experience with composites. However, we used the same fairing shape for the nosecone and truncated it three feet behind the nose. Aft of the nosecone, we will use a cylinder of Coroplast for the body and an angular Coroplast tail. This configuration can be seen in Figure 19, for which we calculated a C_dA of 0.046 and a C_d of 0.131; this is significantly higher than the full fairing. However, this is to be expected, since the modified fairing shape has sharper edges and rougher transitions.

2.4 Steering

In order to determine *Aurora's* steering parameters, we calculated our expected minimum turning radius as a function of velocity. The steering mechanism of bicycles is rather complex, but we chose to consider a simplified system for our calculations. When steering through a curve, a bicycle feels two distinct forces: 1) an outwardly directed centripetal force, and 2) a downwardly directed gravitational force. These forces are illustrated in Figure 20b.

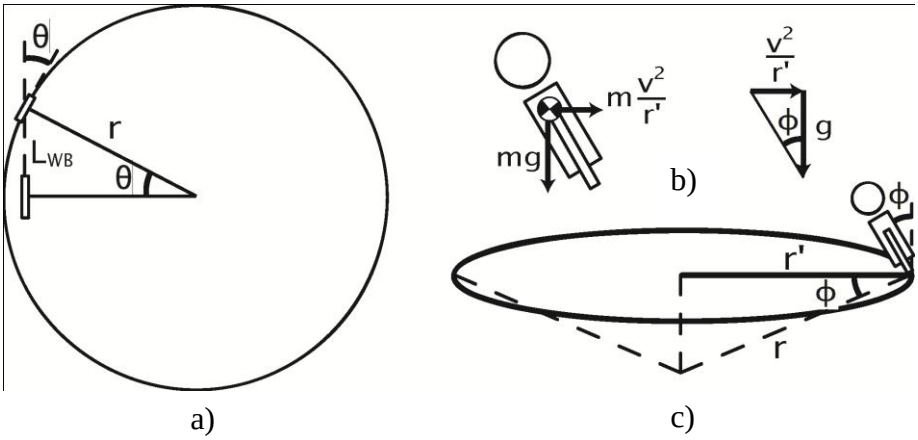

Figure 20: Steering diagrams. In Figure 20a, r is directed into the ground at an angle dictated by lean angle φ; r' represents the effective turning radius.

Gravitation is countered by the normal force, but the lateral acceleration must be countered by the rider. That is, a cyclist must lean into a turn in order to remain in equilibrium. However, when a rider leans at angle φ, neither gravity nor the centripetal force is directed through the system's contact point with the ground. Thus, each force will produce a resultant torque about the contact point. Assuming that the bicycle is a static system, the angular

momentum will be constant, so dL/dt=0. We therefore choose phi such that the sum of torques equals 0. This gives the expression

$$tan(\phi) = \frac{v^2}{r' \cdot g} \tag{1}$$

where r' is the effective turning radius, v is the bicycle velocity, and g is the gravitational constant. By rearranging this, we find an expression for turn radius as a function of velocity and lean angle.

$$r' = \frac{v^2}{g \cdot tan(\phi)} \tag{2}$$

So if we do not lean at all, the turning radius should be infinite (i.e. the bicycle does not turn at all), which makes sense; theoretically, we could also clear a 0 m radius turn by leaning 90 degrees. However, lean angles are limited by the physical shape of the bicycle and rider and also by friction in the tires. At constant velocity and lean angle, a decrease in the turn radius requires an increase in the steering angle. Because of this, the turning radius is also limited by steering capabilities. As we can see in Figure 20a, the steering angle is related to the turn radius by the relation

$$r = L_{wb} \cdot sin(\theta) \tag{3}$$

where L_{wb} is the wheelbase and r is the real turning radius. However, Figure 20c shows that since the bicycle is simultaneously leaning and steering, the turn radius is directed into the ground. Thus, the effective turn radius, r', is defined by the degree of lean.

$$r' = r \cdot cos(\phi) \tag{4}$$

We combine equations (2), (3), and (4) to show that for a given lean angle and velocity there exists a single steering angle theta:

$$\theta = sin^{-1}\left(\frac{L_{wb} \cdot g \cdot sin(\phi)}{v^2}\right) \tag{5}$$

Essentially, this means that we can define a maximum steering angle and a maximum lean angle, and find the resultant minimum turn radius as a function of φ and θ.

$$r' = L_{wb}\frac{cos(\phi)}{sin(\theta)} \tag{3}$$

Steering angle is a function of v and φ, so by fixing either φ or θ, we can find the effective turning radius as a function of speed. Our maximum φ is ultimately limited by the body of the fairing. Based on the CAD model, we estimated that we could lean 30 degrees on a flat plane without touching the ground. With this value, we found the smallest steering angle (16 degrees) that would allow us to clear a 25-foot radius turn, and used this as our limiting θ. Realistically, we expected to construct a vehicle with a larger maximum steering angle than 16 degrees, but this gave us a benchmark for design purposes. Two plots of velocity vs. turn radius were found for a maximum θ and a maximum φ. From these plots, we recorded the higher of the two turning radii, creating a piecewise plot seen in Figure 21. We considered a velocity distribution from 0 to 30 miles per hour, and the wheelbase was estimated to be 2 meters, the longest wheelbase we could expect to have.

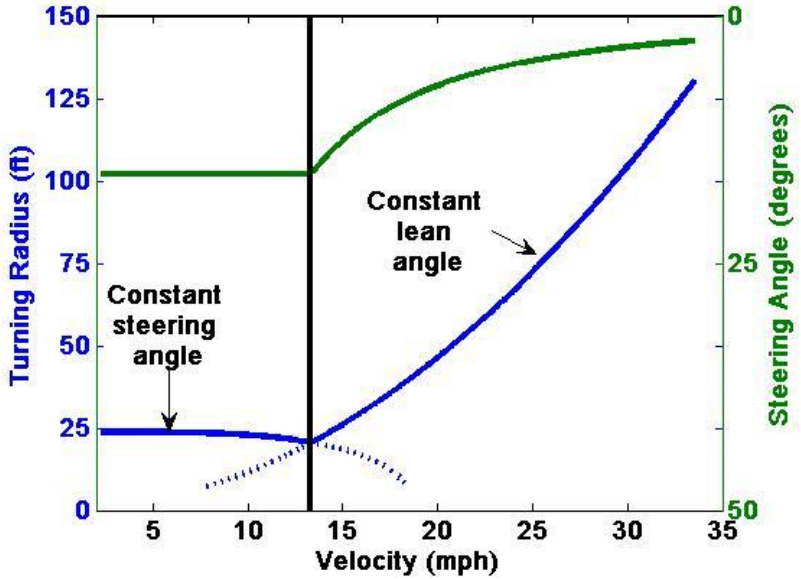

Figure 21: Minimum turn radius as a function of velocity. From 0-13 mph, steering angle is held constant at its maximum value of 16 degrees. From 13-30 mph, the lean angle is held constant at its maximum value of 30 degrees, which causes the steering angle to vary with velocity.

From this, we found that we could clear a 25-foot radius turn at speeds below 15 mph. We therefore concluded that we could meet the ASME specified 25-foot turn radius as long as we could achieve a 16 degree steering angle and a 30 degree lean angle. These parameters yield an optimal turning radius of 21 ft at 13 mph.

2.5 Cost Analysis

Our estimated costs for the building of the *Aurora* vehicle as it was built and for a commercial production run of ten vehicles per month are shown in Table 4. The actual cost of construction was considerably less than the estimate due to donations of fiberglass, epoxy, and many drive train components, as well as the use of components already on hand in place of new purchases.

In the commercial production of *Aurora*, several skilled workers would be responsible for the construction of each vehicle, including all the machining, welding, and composite work. A manager would oversee production and be responsible for supply chain management and other managerial duties. The plug for the fiberglass nosecone could be used to produce at least [check edit] ten nosecones before another plug is required and the frame welding jig can be reused many times, distributing the cost over ten bikes. Also, for a commercial production run, bicycle components and raw materials could be purchased in bulk at wholesale prices, which we assumed to be half of the retail price, as is generally true in bicycle shops. With time, cost efficiency and the production time for the process could be improved considerably.

Single Vehicle Cost Estimation

	Description	Quantity	Unit Cost	Units	Total
	FRAME				
1	Aluminum Thin Walled Tubing	1	$200.00	Lump Sum	$200.00
2	Welding Supplies	1	$20.00	Lump Sum	$20.00
3	Particle Board	2	$15.00	Per Sheet	$30.00
4	Aluminum Blocks	1	$30.00	Lump Sum	$30.00
5	Assorted Hardware	1	$45.00	Lump Sum	$45.00
	NOSE CONE				
7	Epoxy Kit for Nosecone	1	$93.20	Per Kit	$93.20
8	Fiberglass for Plug	10	$12.00	Per Yard	$120.00
9	Blue Foam for Plug	5	$26.64	Per Sheet	$133.20
10	Body Filler	1	$20.00	Per Gallon	$20.00
11	Surface Primer	1	$40.00	Per Gallon	$40.00
12	Assorted Composites Tools	1	$32.75	Lump Sum	$32.75
13	Bondo and Composite Supplies	1	$84.12	Lump Sum	$84.12
	DRIVETRAIN				
14	Shimano Ultegra Components	1	$600.00	Lump Sum	$600.00
15	Rear Wheel	1	$100.00	Per Wheel	$100.00
16	Front Wheel	1	$100.00	Per Wheel	$100.00
				Total	**$1,648.27**

Production Vehicle Cost Estimation

	Description	Quantity	Unit Cost	Units	Total
	LABOR				
1	Machinist/Welder	1	$2,500.00	Per Month	$2,500.00
2	Composite Technician	1	$3,000.00	Per Month	$3,000.00
3	Manager	1	$3,000.00	Per Month	$3,000.00
	BIKE COSTS				
4	Nosecone Plug	1	$430.07	Lump Sum	$430.07
5	Frame Jig	1	$60.00	Lump Sum	$60.00
6	Drive Train Components	10	$400.00	Per Bike	$4,000.00
7	Other Bike Components	10	$179.10	Per Bike	$1,791.00
				Total	**$14,781.07**
				Cost Per Bike	**$1,478.11**

Table 6: Cost analysis chart.

3 Testing

Testing was a critical part of the design process, both before and after fabrication of a working vehicle.

Pre-fabrication Testing

3.1 Weld Testing

In the process of frame analysis we were able to find the stresses placed on the frame, but had no way to be sure of the maximum stresses the frame could withstand. Our initial estimates were based on the accepted yield stress of 4130 chromoly steel with a healthy safety factor for expected weakness around the welded joints. Our first objective

in testing was to better understand the effect of welding on the strength of our joints. To do this, four sections of tube similar to the tube used on the frame were cut, butt welded, air cooled, and later compared to a stock section of the same tube in a tensile test. Each welded section broke as expected, not at the weld, but in the heat-affected area. Surprisingly though, the yield stresses among the tubes were strikingly similar. Many of the stress-strain curves matched the curve of the unwelded tube indistinguishably. Even the more poorly welded tubes with burn-through or low penetration had the same yield stress. From these data we concluded that the strength of the steel around the joints would not be adversely affected by welding. The most significant material effect of welding was a decrease in the breaking strain. This is of minor concern to us though, as the frame is designed to operate in the elastic region only. The yield stresses found in these tests were generally higher than those expected for air-cooled 4130 steel; 520 MPa as compared to 460 MPa for the tabulated value. This is most likely due to the difference in geometry and possibly the manufacturing technique. This result adds a margin of safety to our frame analysis.

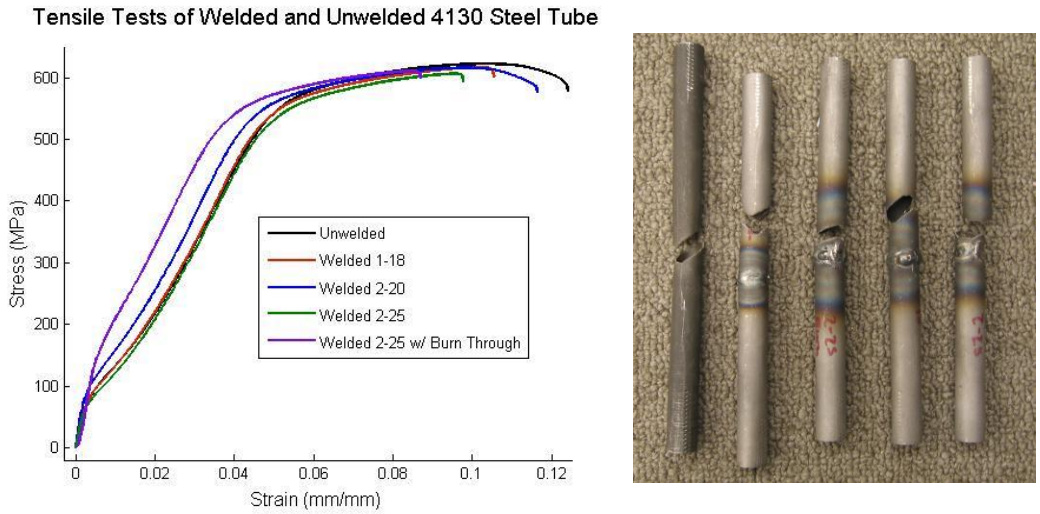

a) Stress-strain curves b) Test specimens

Figure 22: Comparison of welded and unwelded tubes.

Post-fabrication Testing

We optimized many different aspects of our design through practical testing. The ramifications of the results on the design are discussed in detail in the design section. This information was gathered through over 20 miles of test riding to see how the bike handled various conditions as well as check robustness and comfort. During the test ride, we realized that it was difficult to steer the bike with standard handlebars because they interfered with the pedaling motion. Therefore, we tested various alternatives before deciding that a double push-rod was optimal. Similarly, we discovered that the brakes protruded into the path of the knees and adjusted their position. We initially had problems with the chain falling off the jackshaft so we tested many methods of guiding the chain before settling on a roller with the possible addition of plates. These rides also revealed weakness of our initial seat, which plastically deformed, prompting the redesign in steel tubing and mesh.

3.2 Controls

Steering - The turning radius, in the case of this vehicle, is limited not by the steering mechanism so much as by drivetrain interference. Without any interference, the front wheel can turn 17 degrees to the right or 27 degrees to the left, which meets our calculated steering parameters. On a 1.33 m wheelbase, that's a worst case minimum turning radius of 15.8 ft, which is well within the competition's 25 ft radius limitation. Our actual turning radius is even smaller because the measured radius was measured without accounting for lean angle; realistically, we will be moving at speeds that allow us to lean into curves and therefore make tighter turns. With very small amounts of rubbing, we have made turns less than 10 ft in radius.

In terms of passive stability, our prototype frame was built with approximately 1.5 inches of trail; this made it very responsive in turns, but difficult for some of our riders to handle. One major concern is the possibility of front

wheel "shimmy" induced at high speeds. The effect has not been noticed at speeds in excess of 35 mph, but if the front were ever to reach a resonant frequency, the results could be disastrous. In the future version of this frame we will most likely adjust the trail to be closer to 2 or 2.5 inches.

Braking - We tested our brakes to make sure that they complied with the maximum stopping distance specified by the rules. We were able to stop from 15 mph in less than 9 feet, which is well within the 25 feet required. We also measured the stopping distance for a range of other velocities.

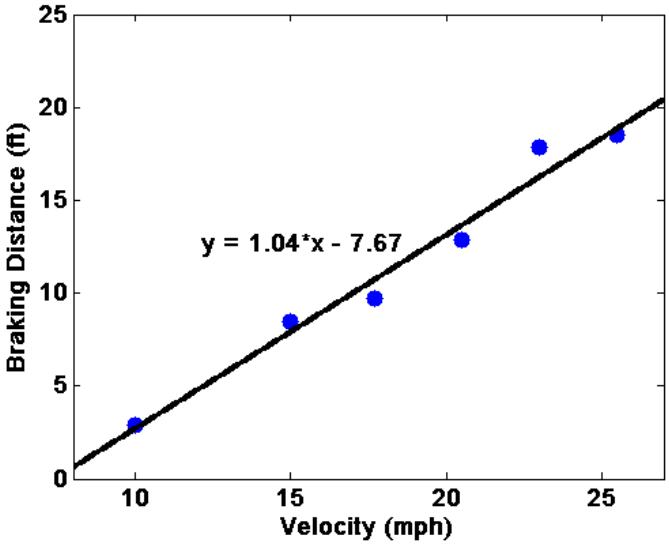

Figure 23: Distance to stop from various speeds

This relation appears to be approximately linear, making the minimum stopping distance from any velocity fairly predictable. The tests were conducted on a dry, flat surface, but at a speed of 25 mph, our rear wheel lifted off the ground about an inch. In this instance, the brakes were applied harder than they would be during normal use and the rider was shifting the center of gravity by leaning forward, but we nonetheless plan to allow for greater stopping distances during competition and general riding.

3.3 Ergonomics and Drivetrain

The *Aurora* was tested on a CompuTrainer ergonometer to determine the maximum power we can expect to produce. The frame was stabilized in a custom jig and the CompuTrainer mounted against the front wheel. On a three mile test one of our riders maintained an average power output of 207 W and achieved a peak power of 516 W. This performance is relatively close to that recorded by Sam Whittingham, Varna Diablo rider, during an 80 mph run in the 2003 World Human Powered Speed Challenge. He was capable of a sustained effort at 250-300W and a peak power of 525 W. This gives us hope that with more practice and some drivetrain adjustments to increase efficiency we will be capable of reaching comparable speeds. Using our theoretical CdA, our peak power output, and the equation

$$\frac{2 \cdot \dot{W}}{C_d A \cdot \rho} = v^3$$

we calculate the theoretical top speed to be 58.9 mph, which would be satisfactory for this competition.

4 Safety

Safety is a necessary consideration for any human powered vehicle designed to travel at high speeds. The design of the vehicle should be such that it minimizes the risk to the rider and bystanders. To this end, we have considered safety in the areas of shell, frame, seatbelt, side protection, roll over protection, and field of view.

Shell material - The fiberglass nosecone and Coroplast shell will fully protect the rider from the road in the case of a crash, saving him or her from abrasion. The shell is also designed to be as aerodynamic as possible and should therefore have a completely smooth surface, posing no threat to bystanders.

Frame material - Steel was chosen as the frame material because of its high strength and fatigue resistance. If our frame were to sustain massive loading, it would only deform, allowing the rider to stop safely, whereas an aluminum frame might be more likely fail catastrophically without prior warning.

Seat belt - The seat will include a structurally attached automotive quality four-point seatbelt harness which will be capable of restraining the rider in case of a high speed flip, preventing injury due to impact.

Side protection - Our roll bar was designed to fully surround the rider so that if the vehicle were to fall on its side the roll bar would contact the ground before the rider's shoulder, dramatically decreasing the severity of the impact.

Roll over protection - The roll bar also extends fully above the rider's helmeted head. If properly fitted in the seat belt the rider should never impact his or her head.

Figure 24: The roll bar is designed to fully surround the rider so that it would be the first to hit in any impact situation.

Field of view - In order to improve the aerodynamics of our vehicle, we did not want the rider's head to rise above the top of the nose cone. This meant that we needed to create a window in our fairing. While peripheral view would remain mostly unobstructed, the rider would need to look past some parts of the steering mechanism and drivetrain in the front of the vehicle. The view would also be temporarily blocked by the rider's knees every rotation of the pedals. However, after many test rides in the same position, we have concluded that the vehicle can be operated safely despite these obstructions.

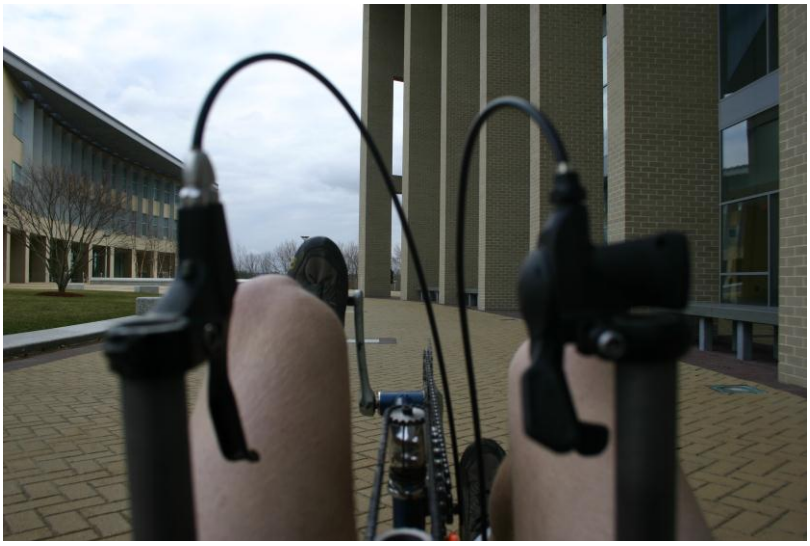

Figure 25: Rider field of view. Though not a completely clear view, it is easy to navigate surrounding obstacles.

5 Summary

To develop the final prototype of the *Aurora* we followed an extensive design process involving rigorous analysis and testing both before and after construction of a working model. We integrated several aspects of highly successful human powered vehicles, improving and innovating where we saw the opportunity. The frame, the most innovative aspect of our design, is characterized by a single horizontal steel tube spanning the distance between the two wheels. This enables a horizontally-adjustable mesh seat to optimize a wide range of comforts and efficiencies for different riders. We chose a front wheel chain drive for its ease of fabrication, robustness, and efficiency, using dual drives to allow the wheel to turn while pedaling. The steering mechanism consists of a double push rod mechanism to maximize knee space without sacrificing sensitivity. Our fairing is a bullet-shaped combination of a fiberglass nosecone and a Coroplast body which reduced cost while maintaining reasonable aerodynamic efficiency.

As part of our analysis, we used computational tools to determine materials, joint strength, fairing shape, and turning radius. We used finite element analysis to predict stresses on joints and decided to use 1.5 inch steel tubing since it was the lightest tubing that met the required FOS. We performed further analysis and found that gussets greatly reduce the stress at the joints while adding minimally to the weight. We analyzed three different fairing designs in CFD to generate pressure distributions and to determine the variation with the lowest drag. We then varied that design to find the optimal nosecone shape. We also calculated the relationship between turning radius and velocity to determine that we could pass the safety inspection provided we were within a few minimum design constraints. From our cost analysis, we figured that these vehicles could be produced for $1,478.11 each.

We tested our vehicle to verify our analysis, safety, and efficiency. We tensile tested multiple pieces of welded steel to conclude that our joints would not be adversely affected by welding, showing the joints could withstand the stresses determined by FEA. After building a working vehicle, we verified that we would more than pass the safety inspection by making a full turn in a 10 ft radius and stopping form 15 mph within 9 feet. Finally, we used a CompuTrainer ergonometer to determine that our drive-train was able to output power comparable to other HPVs and upright bicycles.

We reviewed the designs to insure that our vehicle would be at least as safe as required by ASME standards. The vehicle will include all suggested safety features. By choosing strong materials, accounting for visibility, and designing sound roll over protection, we have insured that our vehicle is safe to ride in the competition.

Olin HPV has created a vehicle that takes a new look at the low-racer recumbent HPV, setting a tone for a promising future as HPV competitors.

Appendix A: Weight Budget

Component	**Weight (lbs)**
Frame	5.938
Front wheel	3.660
Handlebar and controls	1.180
Rear wheel	2.712
Fork	1.459
Brakes	0.463
Jackshaft	0.811
Cranks and pedals	2.474
Derailleur and chain	0.974
Front chain	0.525
Chain tensioner	0.318
Steering assembly	0.617
Bottom bracket	0.710
Seat	5.131
Total	**26.970**

Table 6: Weight Budget.

Works Cited

Beauchamp, Warren. Human Powered Vehicle Graphical Speed Simulator V1.1. 2002. <http://www.recumbents.com/wisil/simul/HPV_Simul.asp#look-up>.

Carroll, D. The Winning Solar Car: A Design Guide for Solar Car Race Teams. SAE International, 2003.

"Dynamic Bicycles." Dynamic Bicycles. Dynamic Bicycles. 08 Apr. 2007 <www.dynamicbicycles.com>.

efluids bicycle dynamics. <http://www.efluids.com/efluids/pages/bicycle.htm >

"MatWeb." MatWeb. 2007. Automation Creations, Inc. 30 Mar. 2007 <http://www.matweb.com>.

Wilson, David G. Bicycling Science. Cambridge: MIT Press, 2004.

“WISIL HPVers”. Beauchamp, Warren. 2006. <http://www.wisil.recumbents.com/wisil/default.asp>.